Post-Print

This is the accepted version of:

When citing this work, cite the original published paper.

Reconstructed Ballistic Data versus Wax Regression-rate Intrusive Measurement in a Hybrid Rocket

Jerome Messineo[1], Koki Kitagawa[2], Carmine Carmicino[3], Toru Shimada[4]

Institute of Space and Astronautical Science, Japan Aerospace Exploration Agency, Japan

Christian Paravan[5]

Aerospace Science and Technology Department, Politecnico di Milano, Italy

Abstract

Burning tests of a laboratory-scale hybrid rocket engine were carried out with gaseous oxygen and a microcrystalline-wax based fuel to look into the feasibility of using an intrusive resistor-based sensor for measuring the fuel regression rate. This initial screening was driven by the need for real-time control of the oxidizer-to-fuel ratio in altering-intensity swirling-flow-type hybrid rocket engines aiming at performance optimization. To build up a framework for comparison with the measured data, a traditional ballistic reconstruction technique was critically revised; with the measured aft-chamber pressure and oxygen mass flow rate time histories, the fuel regression-rate and port diameter were reconstructed over the firing, by estimating the combustion efficiency with the constraint that calculated and measured fuel mass consumed are equal. This technique invariably suffers from the issue of presenting multiple solutions for the fuel mass flow rate in the proximity of the optimum mixture ratio, for which a novel variable-efficiency approach is proposed. Reconstructed data show that regression rate is nearly constant in each firing, yielding dependence upon the port diameter other than the mass flux. Resistor-sensor raw data displayed large deviation from the ballistic results for the slower burning rate of the sensor support. A detailed analysis is presented.

---

[1] Aerospace Project Research Associate, Department of Space Flight Systems, Sagamihara City, Kanagawa 252-5210, Japan; currently Propulsion System and Research Engineer, HyImpulse Technologies GmbH, Wilhelm-Maybach-Straße 5, 74196 Neuenstadt am Kocher, Germany

[2] Assistant Professor, Department of Space Flight Systems, Sagamihara City, Kanagawa 252-5210, Japan

[3] Corresponding author, carmicin@unina.it. Visiting Associate Professor, Department of Space Flight Systems, Sagamihara City, Kanagawa 252-5210, Japan. Currently Baker Hughes, Via Felice Matteucci, 2, 50127 Florence, Italy

[4] Professor, Department of Space Flight Systems, Sagamihara City, Kanagawa 252-5210, Japan

[5] Adjunct Professor, Space Propulsion Laboratory (SPLab), via La Masa 34, 20156, Milan, Italy

Nomenclature

A_t	=	nozzle throat area
a	=	regression rate constant
c^*	=	characteristic exhaust velocity
c_{th}^*	=	ideal characteristic exhaust velocity
c_d	=	nozzle discharge coefficient
D	=	port diameter
D_0	=	initial port diameter
$\widehat{D}_2$	=	final average port diameter
f	=	function of the oxidizer to fuel ratio
f'	=	function of the oxidizer to fuel ratio
f^*	=	function of the oxidizer to fuel ratio
G	=	mass flux
g	=	function of time
L	=	grain length
L^*	=	engine characteristic length
m	=	port diameter exponent
$\dot{m}$	=	mass flow rate
N	=	number of time steps
n	=	mass flux exponent
OF	=	oxidizer-to-fuel mass ratio
O/F	=	overall oxidizer-to-fuel mass ratio
p	=	pressure
R_c	=	gas constant
$\dot{r}$	=	space averaged instantaneous regression rate
t	=	time
t_b	=	burning duration
T_c	=	gas temperature
V_c	=	combustion chamber volume

Greek symbols

η	=	combustion efficiency
η_0	=	combustion efficiency evaluated at O/F
ρ_c	=	gas density
ρ_f	=	fuel density
Ψ	=	function of specific heat ratio
ΔM_f	=	fuel mass consumed
Δt	=	sampling time step

Superscripts

^	=	average in space
−	=	average in time and space

Subscripts

f	=	fuel
ox	=	oxidizer

1.Introduction

Hybrid rockets are chemical propulsion systems which, in the most common configuration, employ a liquid oxidizer and a solid fuel. Yet essentially preserving performance comparable to the most complicated liquid rocket engines, their typical arrangement involves a series of benefits, well known in the propulsion community [1, 2], that can lead to extensive employment as game changing technology in the current space industry [3, 4].

Regression rate of the solid fuel grain is a chief parameter in the operation of hybrid rockets. Thus, predicting the fuel regression rate with accuracy is a fundamental task required in the engine design. Should the accuracy of regression rate estimation be not adequate, rocket performance can significantly deviate from the design, and the overall mission may even be jeopardized [5]. With this purpose, the formulation of a suitable numerical model is still extremely hard and computational-cost demanding [6, 7] for the complexity of phenomena involved in the combustion process occurring in the thrust chamber of these rockets. Laboratory-scale motor firing tests are, hence, necessary to formulate data correlations. Unfortunately, the regression rate measurement in a hybrid rocket is challenging for the harsh combustion chamber environment and the peculiar combustion process. Several experimental techniques have been employed to measure the fuel grain thickness or the port diameter by means of specialized instrumentation, which may be classified as non-intrusive or intrusive. Techniques belonging to the first category make use of sensors that are generally set up outside the motor casing and rely upon ultrasounds or microwaves technology. In both the latter two cases the operating principle is based on the measurement of the waves' time of flight across the solid fuel thickness: the sensor emits waves (ultrasound impulse or electromagnetic wave pulse at the microwave frequency), which travel through the fuel web forth and back, after being reflected at the inner surface of the grain, toward the sensor [8, 9, 10]. X-rays can be used as a non-intrusive measuring system as well [11]. Typically, an instantaneous radiography image is produced by irradiating the combustion chamber with X rays; the sensor measures the intensity of the rays resulting from the passage through the fuel grain providing visual information of the combustion port. However, these techniques, on the one hand, require costly equipment and skilled users, which make them hardly affordable in testing, and, on the other, their application onboard of flying rockets for a feedback control strategy still poses a number of problems.

Sensors of the second category, i.e. intrusive sensors, are implanted in the fuel grain. In general, the sensor may be inserted in the mold before casting of the fuel material or, alternatively, in case the propellant is cast directly in the combustion chamber casing, the sensor may be set up in the casing itself before the material casting. The ideal requisite is that those sensors should not interfere with the fuel consumption mechanism and should burn out together with it, that is, they should neither stick out nor recede with respect to the inner fuel surface. Methods yielding discontinuous measurements of the port diameter during the motor operation were developed by means of probes belonging to this category, which either sense the presence of the approaching burning surface (thermocouples embedded at several radial locations in the fuel grain [12]) or burn out together with the surface regression (electrical circuits which break up instantaneously [13, 14]).

A Resistor Based Sensor (RBS) is a particular type of such a class of probes whose construction details are shown later: it is embedded in the fuel grain and delivers an electric voltage proportional to the fuel web thickness. The SPLab (Space Propulsion Laboratory) from Politecnico di Milano developed its own RBS technology [15], and together with JAXA a collaboration has been established in order to study this type of measurements specifically for the application to the control of an A-SOFT (Altering-intensity Swirling-Oxidizer-Flow-Type) engine [16]. Such a hybrid rocket engine employs a combination of both axial and swirling oxidizer mass flow injections, which need to be throttled in a feedback loop to

overcome the natural shift of the oxidizer to fuel ratio and independently control the rocket thrust, optimizing performance. For this reason, instantaneous accurate in-flight fuel mass flow rate measurement is required [17]. With this regard, the main shortcoming of a RBS system is that it is able to provide only average values of the regression rates over time periods which cannot be chosen too short (because of the precision of the measure) and, on the other side, cannot be too long (because of the substantial changes in the thermo-fluid dynamic conditions in the combustion chamber). Nevertheless, it is much cheaper, lighter and affordable than the complex devices mentioned above, for which its application deserves careful attention.

In this paper, on the one hand, the results of a series of firing tests of a small-scale laboratory hybrid rocket engine burning gaseous oxygen with a kind of paraffin-based fuel grains are reported. Paraffin-based fuels are, in fact, of utmost interest for their larger regression rate in comparison to traditional polymers (see for example Ref. [18]). With this class of materials, fuel is consumed not only by gasification but, because of the formation of a low-viscosity unstable melt layer on the burning surface, fuel liquid droplets and/or filaments are entrained into the main gas stream [19, 20], by substantially raising the solid regression rate. This phenomenon is caused by the liquid layer instability, which is affected by the fuel composition and its thermo-mechanical properties [21] that can significantly change depending on the specific fuel formulation, the manufacturing process and the motor operating conditions. As a consequence, the behavior of paraffin-based fuels is hardly predictable [22]. The engine static firings were aimed at testing an RBS version previously designed for standard polymeric fuels in several operating conditions to identify the limitations and the quality of the measurement method with a liquefying fuel. On the other hand, an existing ballistic data reconstruction technique is reconsidered and critically revised with the purpose of building space-averaged regression rate and port diameter evolutions in the firing, for a comparison with the RBS output. In this framework, thus, the reconstructed data have the twofold function of, first, posing a base for comparison, and, second, analyzing the rocket internal ballistics for a more general data-correlation purpose.

2. Regression Rate Measurement Sensor

In Figure 1 a schematic drawing of the resistor sensor arrangement is shown; the sensor is composed of seven conductor-resistor (R_i, i=1...7) pairs connected in parallel with each other and in series with the resistor R, mounted on a fiberglass epoxy resin support of 0.8-mm thickness. The conductors, of 0.1-mm diameter, are laid down on the support surface.
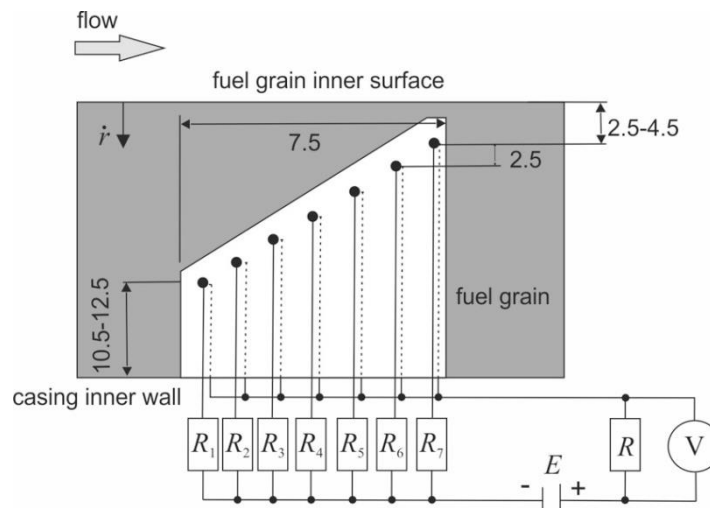

Figure 1 RBS electrical circuit and installation schematic (dimension are in mm).

4

The electrical circuit is powered by an external battery, *E*, delivering 9 V, with a total absorbed power around 10 mW. While the fuel grain is consumed, its inner surface moves approaching the conductors, which are successively burned through; the parallel arrangement of the conductor-resistor pairs is then modified as well as the overall resistance value of the circuit. It follows that, each time a conductor breaks, the electric current through the sensor circuit is modified. Therefore, the electric tension, *V*, measured across the resistor *R*, is changed and, assuming that the solid grain surface and the conductors regress with the same rate, the instantaneous position of the solid fuel surface can be deduced from the position of each conductor with respect to the casing inner wall and initial inner surface of the port.

3.Experimental Set-up and Data Reduction Technique

A cross section of the laboratory-scale engine is shown in Figure 2. All the components are made of SUS304 stainless steel, except the converging nozzle, which is made by a massive block of oxygen-free copper with a throat diameter of 14 mm. The forward closure flange of the engine is equipped with a dual injector assembly consisting of an axial injector plate with eight ports of 3-mm diameter each equally spaced on a circumference of 32.5 mm diameter, and a tangential injector plate with eight slits; however, in this experimental campaign only the axial injector is used (the tangential injection port is plugged).

Single-port solid-fuel grains made of microcrystalline wax[*] (HiMic 1080 provided by Nippon Seiro Co. Ltd.) with 40 mm nominal initial port diameter are used; the latter is equal to the inner diameter of the prechamber that accommodates the injector plate. Grains were cast directly in the combustion chamber to allow embedding the resistor sensor as shown in Figure 2. The microcrystalline wax was melted up to 120°C and mixed with 20% by mass of stearic acid (material components' properties are listed in Table 1). The liquid mixture was, then, poured in the combustion chamber which was preheated to 120°C along with the central rod. To remove the bubbles in the liquid wax, vacuum (around 10 kPa) was made in the chamber for about 15 min. After that, the chamber was pressurized with nitrogen to 0.6 MPa. The duration of the system cooling down was controlled with temperature regulators to last around 5 hours. The average fuel grains' density measured after the test over the grains was 899.5 kg/m^3,with a percent difference with respect to the theoretical maximum density of less than 4%.

Table 1 Fuel components' properties (as declared by the material supplier).

Material	Melting point °C	Density kg/m^3	Kinematic viscosity mm^2/s
HiMic 1080	84.2	931@25°C 792@100°C	14.87 @100°C
Stearic acid	68-71	941@20°C 847@70°C	5.85@40°C

The regression-rate sensor is placed in the grain mid length; it is assembled into an NPT male connector in SUS316 that is screwed in the combustion chamber casing.

---

[*]There are two major classifications of waxes: paraffin that forms large, defined crystalline structures, and micro-crystalline waxes, which have more branched chains and much smaller crystals of irregular shape. Micro crystalline wax consists of high molecular-weight saturated aliphatic hydrocarbons. It is generally darker, more viscous, denser, tackier and more elastic than macro-crystalline waxes, and has a higher molecular weight and melting point.
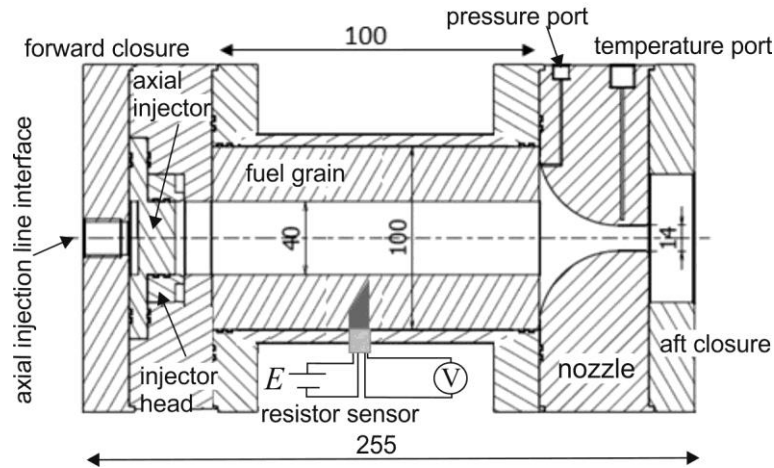
Figure 2 Hybrid rocket engine cross section (dimensions are in mm).

The nozzle is equipped with a pressure tap to measure aft chamber pressure and a thermocouple port to control the temperature inside the nozzle for safety reasons. Oxygen mass flow rate is measured with a calibrated choked orifice (with 2.6 mm diameter) placed just upstream of the injector (see Figure 3). Cold flow tests were carried out to measure the discharge coefficient of the orifice in the various combustion test configurations. Injection pressure, i.e. downstream of the orifice, is measured by means of a dedicated pressure transducer. Also, a turbine flow meter is installed on the oxygen feeding line for redundancy of the measurement and to capture the unsteady phases when the orifice is not choked.

Engine ignition is achieved by applying 12 V voltage to a nichrome wire glued on the inner surface of the grain at the inlet section; oxygen is supplied for the ignition through a dedicated line with a flow rate adjusted to about 0.1 g/s with the supply pressure main valve and the opening degree of a needle valve.

Engine extinguishment is obtained by closing the main oxygen valve and switching to nitrogen supply.
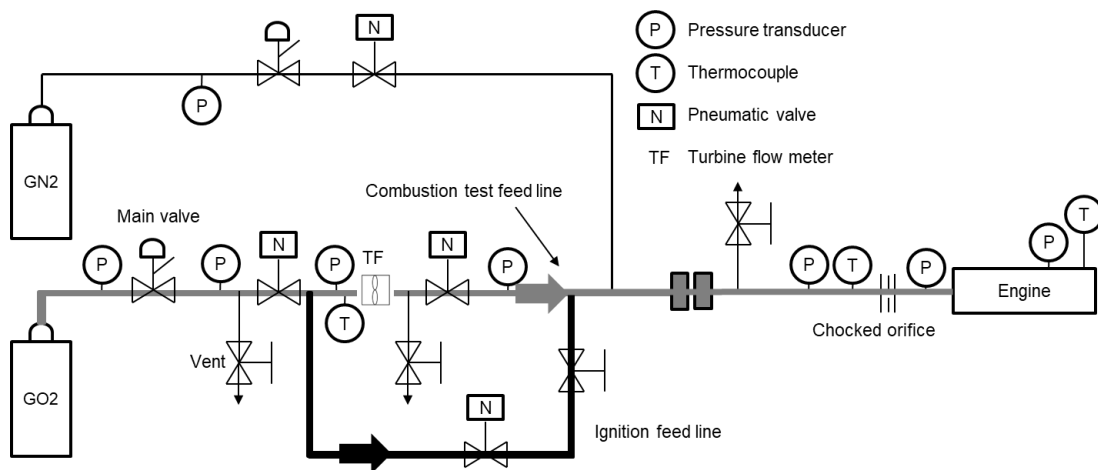

Figure 3 Schematic of feed lines and instrumentation diagram.

Signals from the sensors were first amplified and then converted from analogue to digital data by the analog-to-digital converter (ADC); by means of a dedicated software developed in LabView 2013 SP1, the digital voltage data from the ADC and their corresponding data transformed into physical units were recorded on the computer at sampling rates of 1000 Hz and 10 Hz (sampling time step $\Delta t = 0.1$ s), respectively, the latter after averaging the output voltages over 100 points. The

regulators and needle valves were manually adjusted to set the initial oxidizer feed pressure, purge gas pressure, and flow rate of the oxidizer for ignition. The three pneumatic ball valves enabled the manual and automatic control of the oxidizer and purge flows. The control program controlled the solenoid valves that operated the pneumatic valves and the igniter via a relay unit.

3.1 Experimental Test Conditions and Average Data Definition

A total number of seven firing tests were planned as shown in Table 2. Two preliminary tests, called ignition tests (I#), were scheduled to check the overall functionality of the experimental test facility as well as the mechanical behavior of the microcrystalline wax grains; they were carried out without embedding the regression-rate sensor into the grains. In those cases, the sensor housing on the casing was properly plugged. The remaining five tests, called firing tests (F#), were designed to ensure that the last conductor of the sensor is reached before the engine shut down. Regression rate was estimated based on the data available in Ref. [23]. Finally, test F#05 was dedicated to check the repeatability of the results.

Table 2 Test matrix definition.

Test	Oxygen mass flow rate, kg/s	Burning duration, s	Notes
I#01	0.02	5	Ignition tests to check experimental facility functionality
I#02	0.04	5	
F#01	0.02	22	RBS was installed on the bottom of the casing as in Figure 2
F#02	0.03	18	After test F#01, RBS installation changed to the top of the casing
F#03	0.05	5	
F#04	0.05	13	
F#05	0.03	18	Repetition of F#02 to check firing repeatability

Note that the nominal burning time in Table 2 is actually the time period in which the main oxygen feeding valve is open, and thus the effective burning duration is larger for the valve inertia.

The average parameters in every firing test were calculated with the classical fuel-mass loss method. The time-average fuel mass flow rate, $\bar{m}_f$, is determined by dividing the measured fuel mass loss ΔM_f by the burning duration, t_b:

$$\bar{m}_f = \frac{\Delta M_f}{t_b} \tag{1}$$

The burning duration follows from the pressure time history (see Figure 4), by identifying the inflection point on the first main rise portion of the pressure trace (initial burning instant) and that on the end decrease portion (final burning instant).

The port diameter averaged over the entire burning, $\bar{D} = \left(D_0 + \hat{D}_2 \right)/2$, is determined starting from the initial port diameter D_0 and the final one, $\hat{D}_2$, averaged over the grain axis. The latter is estimated via the consumed fuel mass assuming that the cylindrical shape is preserved after the combustion:

$$\widehat{D}_2 = \sqrt{D_0^2 + \frac{4}{\pi} \frac{\Delta M_f}{\rho_f L}} \qquad (2)$$

Finally, the time and space averaged regression rate is, by definition:

$$\bar{\bar{r}} = \frac{\widehat{D}_2 - D_0}{2t_b} \qquad (3)$$

and the average mass flux, either if it is the oxidizer or the total one, is referred to the average port section area calculated with the above-mentioned average port diameter in the burn. The mean oxidizer to fuel mixture ratio is evaluated as the ratio between the average oxygen mass flow rate in the burn and the average fuel mass flow rate previously defined:

$$O/F = \frac{\bar{\bar{m}}_{ox}}{\bar{\bar{m}}_f} \qquad (4)$$

The average combustion efficiency, η_0, is defined as the ratio of the experimentally measured average characteristic exhaust velocity, $\bar{c}^* = (\bar{p} A_t)/(\bar{m}_{ox} + \bar{m}_f)$, to the corresponding ideal value, $\bar{c}_{th}^*$, which was computed with the CEA chemical equilibrium code [24] at the effective mean pressure $\bar{p}$ and mean oxidizer to fuel mixture ratio O/F assuming frozen conditions through the nozzle:

$$\eta_0 = \frac{\bar{c}^*}{\bar{c}_{th}^*} \qquad (5)$$

However, average data in the firing are not useful for a comparison to the port diameter measured with the regression-rate sensor in the burning. A method capable of reconstructing the regression rate as a function of time and the port diameter evolution is required. With this purpose, a ballistic data reconstruction technique was implemented, which allows determining the time-resolved space-average regression rate and port diameter starting from the measured oxygen mass flow rate and chamber pressure; the details are addressed in the next section.

Typical oxygen and chamber pressure time histories measured in a firing test are depicted in Figure 4a; here, the main-valve open state was from 0 to 18 s, and the estimated ignition and extinguishment instants are 0.3 and 19.4 s respectively, with a total burning time of 19.1 s.
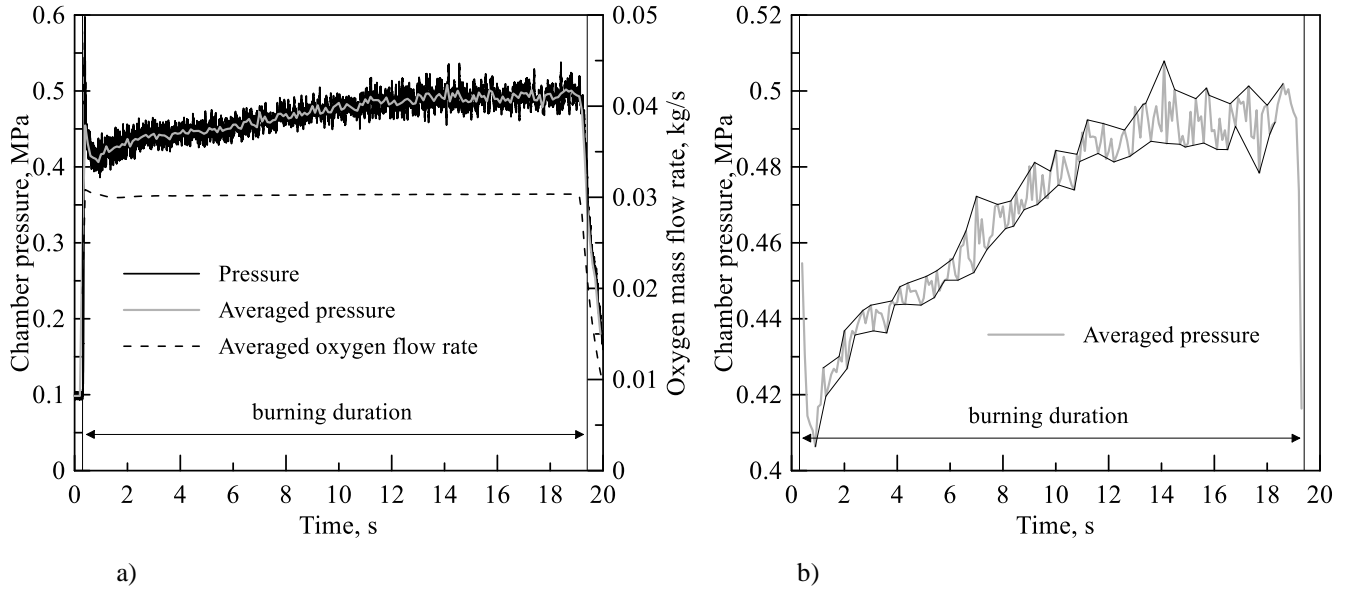
Figure 4 Test F#02: a) chamber pressure and oxygen mass flow rate, b) average pressure oscillation envelope.

The pressure and mass flow rate data averaged over 100 points are used for the reconstruction technique; zoomed in data are plotted in Figure 4b with the envelopes of minimum and maximum points, which highlight the increase of pressure oscillation amplitude over time.

3.2 Ballistic Data Reconstruction Method

Hybrid rocket competent literature presents a class of methods developed to obtain the time-resolved space-averaged regression rate, which rely upon internal ballistics reconstruction techniques [25]. Basically, with, at least, the oxidizer mass flow rate and post-combustion chamber pressure measurements, one can estimate the space-averaged regression rate at each instant over the engine firing. These methods either assume an average combustion efficiency in the burn [26, 27, 28] or attempt to determine this latter by additionally measuring the motor thrust [29], and are all based on the statement of the mass balance inside the combustion chamber. Another more sophisticated technique makes use of the additional measurement of the pressure level in the motor prechamber and allows evaluating the combustion efficiency evolution over the burning time as well [30]. Post-test measurement of the solid fuel mass consumed is required by all the reconstruction procedures, which, thus, hinders a real-time estimation of regression rate.

Here, the most basic of those techniques is discussed and applied to the determination of the time-resolved space-averaged port diameter. With the introduction of the characteristic exhaust velocity efficiency, η,

$$\eta = \frac{c^*}{c^*_{th}} \tag{6}$$

the following form of the mass conservation equation is obtained by imposing that the sum of the oxidizer mass flow rate injected into the chamber and of the fuel mass flow rate stemming from the solid grain consumption is equal to the mass flow rate discharged from the exhaust nozzle, plus the time rate of change of the mass contained in the volume of the combustion chamber:

9

$$\dot{m}_{ox} + \dot{m}_f = c_d \frac{pA_t}{\eta c_{th}^*} + \frac{d}{dt}(\rho_c V_c) \qquad (7)$$

being V_c the overall volume of the prechamber and fuel grain port, and ρ_c the gas density. c_d is the nozzle discharge coefficient that accounts for the non-one-dimensionality and non-isentropicity of the flow, which, by narrowing the effective cross sectional area, tend to reduce the actual mass flow rate compared to the one in the ideal equivalent flow [29]. Assuming an isothermal process, and expressing the product of the average chamber temperature, T_c, and gas constant, R_c, in terms of the characteristic exhaust velocity, $R_c T_c = \alpha(\eta c_{th}^*)^2 \Psi^2$, through the proportionality factor α that takes into account temperature and gas composition non-uniformity across the chamber, one obtains:

$$\dot{m}_{ox} + \dot{m}_f \left(1 - \frac{\rho_c}{\rho_f}\right) = c_d \frac{pA_t}{\eta c_{th}^*} + \frac{V_c}{\alpha(\eta c_{th}^*)^2 \Psi^2} \frac{dp}{dt} \qquad (8)$$

where Ψ is a function of the specific heat ratio [31], and both its value and α are on the order of 1.

In the current investigation dealing with quasi-steady regression rate estimation, the time derivative appearing in Eq. (8) has to be intended as the time variation of the slow-varying chamber pressure, which, assuming a linear pressure increase, can be readily estimated from Figure 4 to be around 0.005 MPa/s. The order of magnitude of the unsteady term in the mass balance equation relative to the steady mass flow rate is, thus, given by $(L^*/c_{th}^*) \, dln(p)/dt \ll 1$, which can be definitely neglected, leading to the quasi-steady form:

$$\dot{m}_{ox} + \dot{m}_f = c_d \frac{pA_t}{\eta c_{th}^*} \qquad (9)$$

in which the ratio of the gas to solid fuel density, $\rho_c/\rho_f \ll 1$, appearing in the Eq. (8) as a consequence of the enlargement of the fuel port over time, has been ignored.

Eq. (9) holds all over the engine operation (except for the ignition and final shut down unsteady phases), and each term has to be considered depending on time. Note that here the nozzle throat area is constant. The ideal characteristic velocity is essentially a function of the instantaneous overall mixture ratio $OF = \dot{m}_{ox}/\dot{m}_f$, being the chamber pressure variation in a single firing test so small that the relative variation of c_{th}^* can be neglected. Also, by neglecting the two-phase flow effects of non-burned liquid wax crossing the nozzle, the discharge coefficient is a function of the total mass flow rate exhausted from the engine by virtue of the nozzle-throat Reynolds number, which yields meaningful variation only by orders-of-magnitude change of the Reynolds number [32]. In practice, it can be considered constant in the firing test for the small variation of the total mass flow rate. Typical values of the nozzle-throat Reynolds number and discharge coefficient in a test are $4 \cdot 10^4 \div 8 \cdot 10^4$ and 0.99, respectively; the latter, thus, accounts for around 1% larger value of the calculated efficiency.

For convenience, Eq. (9) can be rearranged to separate out the terms explicitly depending on time, on the right hand side of Eq. (10), from those essentially depending on the mixture ratio, which are grouped on the left hand side:

$$c_{th}^* \left(1 + \frac{1}{OF}\right) = c_d \frac{pA_t}{\eta \dot{m}_{ox}} \qquad (10)$$

here pressure and oxidizer mass flow rate are measured quantities. Hence, the engine mixture ratio, OF, can be calculated by solving Eq. (10) once the efficiency is assigned. As will be addressed in the following, the solution of Eq. (10) can be tricky, more or less depending on the propellant selection, because of the shape of the function $f(OF)$, which is defined in Eq. (11):

$$f(OF) = c_{th}^*(1 + 1/OF) \qquad (11)$$

The ideal characteristic velocity, c_{th}^*, is computed at the mean chamber pressure measured over a given test; the fuel is modeled as composed of 80% by mass $C_{32}H_{66}$ with molecular weight equal to 450.88 g/mol and heat of formation equal to -967.8 kJ/mol [33], and 20% $C_{18}H_{36}O_2$ (stearic acid) with molecular weight equal to 284.484 g/mol and heat of formation equal to -947.7 kJ/mol [34]; gaseous oxygen is supposed to enter the chamber at 300 K. The results of the computations carried out at two different chamber pressure levels including the low and high limits of the experimental data range are shown in Figure 5 along with the percent deviation between the two.
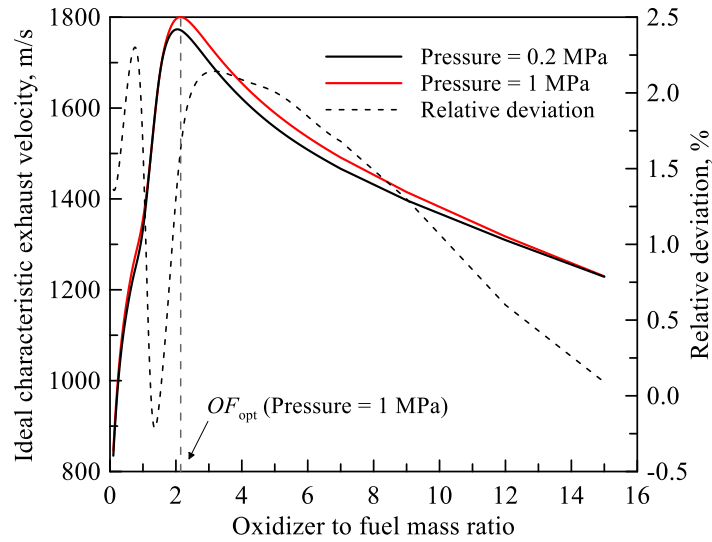

Figure 5 Ideal characteristic exhaust velocity as a function of the mixture ratio calculated at 0.2 and 1 MPa.

A maximum deviation of 2.3% is yielded with a five-fold pressure increase, which justifies the choice of considering c_{th}^* independent of pressure in a single firing.

The diagram of the function $f(OF)$ obtained at 0.5-MPa chamber pressure (that is the mid-range of pressures referred to in Figure 5) is depicted in Figure 6. The solution of Eq. (10) at each time step consists in finding the roots of the function $f(OF) - g(t)$, where $g(t)$ is defined in Eq. (12):

$$\mathrm{g}(t) = c_d \frac{pA_t}{\eta \dot{m}_{ox}} \qquad (12)$$
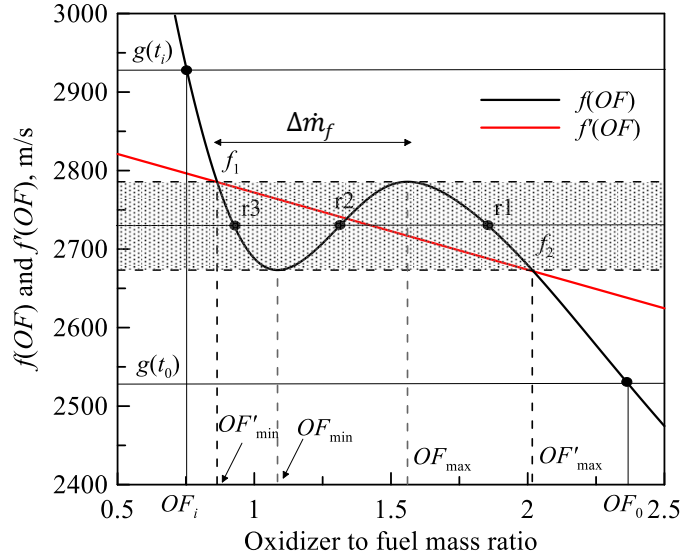
11

Figure 6 Graphical representation of the method of solution of Eq. (10).

It is clear that in a wide range of oxidizer to fuel mass ratios the function $f(OF)$ is not monotonic, yielding both a minimum and a maximum point at $OF_{min}= 1.085$ and $OF_{max}= 1.560$, respectively. Thus, in the range of mixture ratios $OF'_{min}= 0.864$, $OF'_{max}= 2.012$, Eq. (10) shows three distinct solutions. It is worth noting that this behavior always occurs in a left interval in the neighborhood of the optimum oxidizer to fuel ratio, OF_{opt} (see Figure 5), as can be readily seen by deriving the function f with respect to OF:

$$\frac{df}{dOF} = 0 \Leftrightarrow \frac{1}{c_{th}^*}\frac{dc_{th}^*}{dOF} - \frac{1}{OF^2 + OF} = 0 \tag{13}$$

From Eq. (13) it appears that, regardless of the propellant combination, because the ideal characteristic velocity peaks at the optimum mixture ratio, two points, OF_{min} and OF_{max}, exist where the derivative of the function f is null, and this happens on the increasing branch of the c_{th}^* curve ($dc_{th}^*/dOF > 0$). The magnitude of the difference $OF_{max} - OF_{min}$ depends on the shape of c_{th}^*. As hybrid rockets are usually designed to operate around the point maximizing the specific impulse, even though the latter is somewhat higher than the optimum mixture ratio, it is likely that the OF shift in the engine firing falls close to or in the above-mentioned range. This feature has been heuristically pointed out in Ref. [28] and, actually, it might not be a problem inasmuch as the values attained by the function $g(t)$ over the firing definitely lie all either below f_1 or above f_2 (i.e. outside the shaded rectangle in Figure 6). In fact, in the latter two events, in case of three roots (i.e. $g(t) \in [f_1, f_2]$), with a root tracking procedure one might follow the proper solution by assuming the actual root at time $t+\Delta t$ is that of the three possible ones (r1, r2, r3 in Figure 6) which is the closest to the root at time t. The real problem is that, for the pressure increase in the firing (see Figure 4), the values of the function $g(t)$ can span in a range including both f_2 and f_1. In particular, at the engine ignition, $g(t_0)$ is typically lower than f_2, and it increases with time, exceeding f_1 at some time t_i. In this case, the calculated OF will tend to decrease over time, shifting up to OF'_{max}; after that, with a further increase of $g(t)$, by selecting the proper root, r1, in the range $[OF'_{max}, OF_{max}]$, at the time instant when $g(t) > f_1$, it will suddenly shift left to a value lower than OF'_{min}, thus yielding an unphysical discontinuity of the calculated fuel mass flow rate approximately given by $\Delta\dot{m}_f \cong \dot{m}_{ox}\left(\frac{1}{OF'_{min}} - \frac{1}{OF_{max}}\right)$. Of course, in case of decreasing pressure in the firing, such that $g(t)$ spans in an equal

12

range of values, first the solution r3 is selected up to OF_{min}, and, then, a jump in the calculated OF will equally occur when $g(t) < f_2$. In the latter instance, the fuel mass flow rate discontinuity will be different in magnitude: $\Delta \dot{m}_f \cong \dot{m}_{ox} \left(\frac{1}{OF_{min}} - \frac{1}{OF'_{max}} \right)$.

In the current modeling framework, this unphysical behavior results from arbitrarily assuming constant efficiency; it is, indeed, known that in hybrid rockets this assumption may be weak because of the variable propellant mixing conditions establishing in the burning [29, 30]. Here, a simple method is employed to overcome this issue, which consists in substituting the function $f(OF)$ with a linear interpolation, $f'(OF)$, in the range $[OF'_{min}, OF'_{max}]$, as represented by the grey dashed line in Figure 6; thus Eq. (10) is formally substituted by $f^*(OF) - g(t) = 0$, where the function $f^*(OF)$ is defined below

$$f^*(OF) = \begin{cases} f(OF), \forall OF \notin [OF'_{min}, OF'_{max}] \\ f'(OF), \forall OF \in [OF'_{min}, OF'_{max}] \end{cases} \tag{14}$$

Note that, this approach is equivalent to supposing that, in the above-mentioned oxidizer to fuel mass ratios, the efficiency is not constant, but proportional to η through the ratio $f'(OF)/f(OF)$ between the linear interpolation f' and the function f (see Figure 6). A similar approximation was proposed in Ref. [35] with the application of a different data reconstruction technique for estimating the nozzle throat erosion, even though the range of OF in which the interpolation is applied is not specified. However, every continuous function monotonically decreasing in $[OF'_{min}, OF'_{max}]$ and equal to f_1 and f_2 at the extremes of the interval, respectively, can be selected. The influence of different functions is discussed in the Appendix.

Hence, in summary, if $\forall\ t \in [0, t_b]\ g(t) \in [g_1, g_2]$ with $[f_1, f_2] \subset [g_1, g_2]$, the function f is substituted with f^*, otherwise the root tracking procedure addressed above is implemented.

Once the mixture ratio OF_i at the time step $t = t_i$, is computed, the fuel mass flow rate, the spatially averaged regression rate and the updated average port diameter are calculated as follows:

$$\dot{m}_{f_i} = \frac{\dot{m}_{ox}}{OF_i} \tag{15}$$

$$\dot{r}_i = \frac{\dot{m}_{f_i}}{\rho_f \pi D_i L} \tag{16}$$

$$D_{i+1} = D_i + 2\dot{r}_i \Delta t \tag{17}$$

in which the used time step is related to the sample rate, i.e $\Delta t = 0.1$ s, and it is believed small enough to permit a forward Euler integration with negligible error. Iterating this procedure until extinguishment, the total fuel mass consumed $\Delta M'_f$ is computed as the integral of fuel mass flow rate over the burning time (split in N time steps):

$$\Delta M_f' = \sum_{i=1}^{N} \dot{m}_{f_i} \Delta t \tag{18}$$

This term, in the present scheme, is a function of the assumed efficiency, η, that is the unknown of the problem. The latter is found by imposing that the fuel mass consumed is equal to the measured one, ΔM_f, i.e. by solving the following equation for η:

$$\Delta M_f'(\eta) = \Delta M_f \tag{19}$$

The relative deviation between the calculated fuel mass, $\Delta M'_f$, and the measured one, ΔM_f, in the firing F#02 is reported as a function of the efficiency in Figure 7. Here, the black solid curve has been traced by solving Eq. (10) at each time step in the firing considering the function $f(OF)$ all over the efficiency range considered in the plot; whereas, the grey dotted line has been obtained considering the function $f^*(OF)$, for comparison. In the range of physically acceptable efficiencies, the function (calculated in either way) is monotonically decreasing, as can be explained noticing that, by raising the efficiency, the function $g(t)$ decreases, leading to higher OF ratios in the firing (see Figure 6) and, consequently, to lower fuel mass flow rates. With the same argument one can recognize that, for $\eta < 0.73$ and $\eta > 0.95$, the two curves are perfectly overlapped as the values of $g(t)$ are all increased above f_1 and decreased below f_2, respectively, allowing for uniquely defined OF values ($f^* \equiv f$).
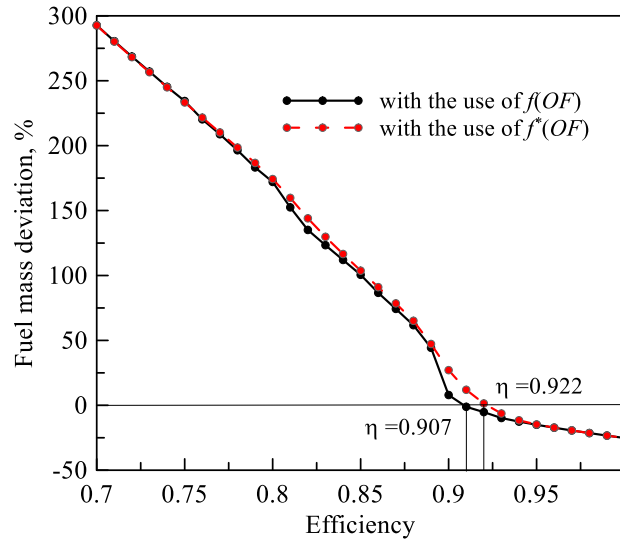

Figure 7 Percent deviation of calculated fuel mass compared to the measured one (Eq. (19)) in the firing F#02.

In Figure 8a the calculated time trends of the oxidizer to fuel mass ratio corresponding to the two curves in Figure 7 are plotted. Incidentally, note that the oxidizer-to-fuel ratio characteristic values (represented by the horizontal lines in the figure) are slightly different from those shown in Figure 6 for the yet small chamber pressure difference of test F#02. Note that, even though the derived regression rates are slightly different (Figure 8b), the final port diameters obtained with both trends are, of course, equal, since both fuel mass flow rate histories satisfy Eq. (19), albeit with two different efficiency values (i.e. those reported in Figure 7). Moreover, the deviation between the calculated OF values existing even for $OF > OF'_{max}$ (i.e. when $t < 10$ s) is due to the scaled values of the function $g(t)$ with the two different efficiencies.
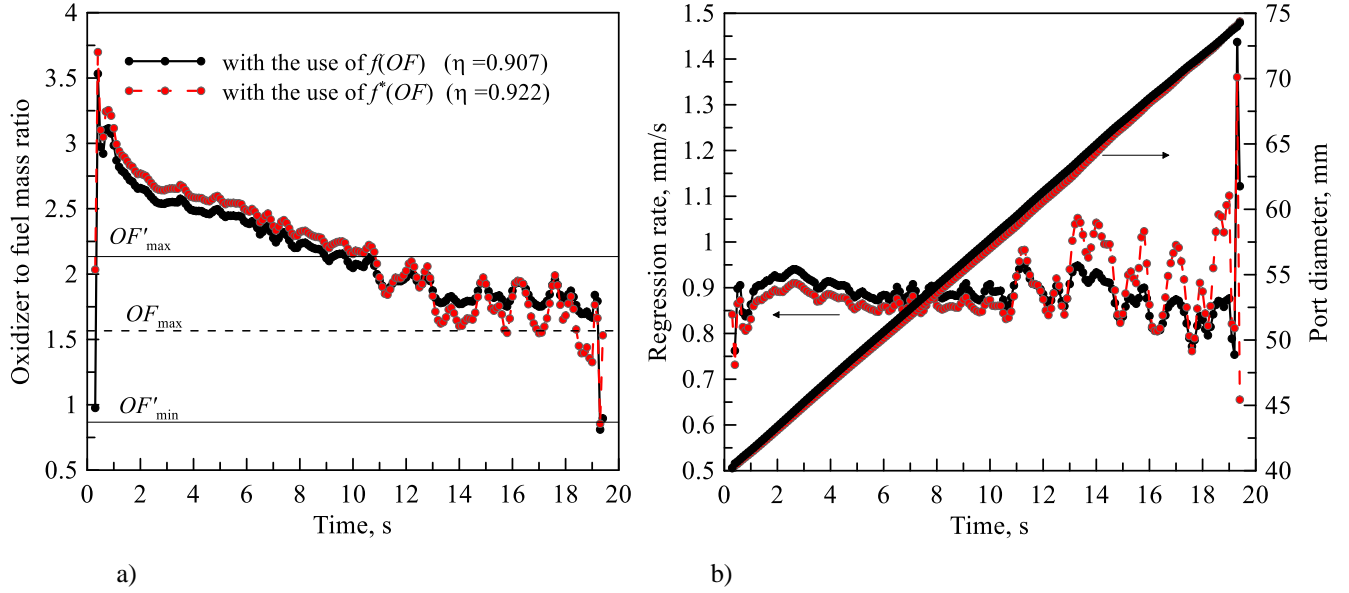
14

Figure 8 Time histories in the firing F#02 of a) oxidizer to fuel mass ratio, b) regression rate and port diameter.

In this specific case, with $\eta = 0.907$ (that is the solution of Eq. (19)), the calculated OF values are all larger than OF_{max}, except in the last two points at the end of the burn; accordingly, by searching for the solution of Eq. (10), the root r1 on the branch of the function f in the interval $[OF'_{max}, OF_{max}]$ has been selected up to the engine shut down when both oxygen mass flow rate and pressure are decreased. After that, in fact, a discontinuity from $OF > OF_{max}$ to $OF < OF'_{min}$ is produced. The fluctuations of regression rate clearly appearing in Figure 8b 10 seconds after the ignition (i.e. in the range $[OF'_{max}, OF_{max}]$) are larger if calculated with the function f^* (grey curve). Those fluctuations are naturally related to (but not physically caused by) the chamber pressure fluctuation (see Figure 4b) and, eventually, to the corresponding variation of $g(t)$. To see the reason why they are amplified when f^* is used instead of f, consider the percent variation of regression rate relative to the corresponding variation of pressure in a time step:

$$\frac{\Delta \dot{r}}{\dot{r}} \Big/ \frac{\Delta p}{p} = -g(t) \cdot \begin{cases} \dfrac{1}{OF}\dfrac{1}{df/dOF} \\ \dfrac{1}{OF}\dfrac{1}{df^*/dOF} \end{cases} \tag{20}$$

in which the variation of port diameter was neglected and $\Delta\dot{r}/\Delta p \cong d\dot{r}/dp$. In the considered OF range the derivatives of f and f^* are both negative, so that pressure and regression rate variations have equal sign. Furthermore, in the same range, the derivative of f is variable and, on average, larger than that of f^* or, equivalently, of f' that is, instead, a constant (see Figure 6), as well as the calculated OF, which explains the higher level of regression rate fluctuations. Notice that Eq. (20) by no means represents the so-called regression-rate pressure-coupled response function, which would entail a cause-effect concept between pressure fluctuations and related regression rate oscillations; we remark that it rather establishes a relationship between the measured pressure signal and the reconstructed regression rate.

However, the deviation between the port-diameter evolutions calculated in the two ways is practically negligible. The main conceptual difference between the two sets of results, as mentioned above, is that resorting to the function $f^*(OF)$ implicitly involves an efficiency variation in the range $[OF'_{max}, OF_{max}]$, which is plotted in Figure 9 in terms of the ratio ξ:

15

$$\xi_i = \frac{pA_t}{\eta \dot{m}_{ox}} \frac{c_d}{c_{th}^*(OF_i)\left(1 + \frac{1}{OF_i}\right)} = \frac{f^*(OF_i)}{f(OF_i)} \qquad (21)$$
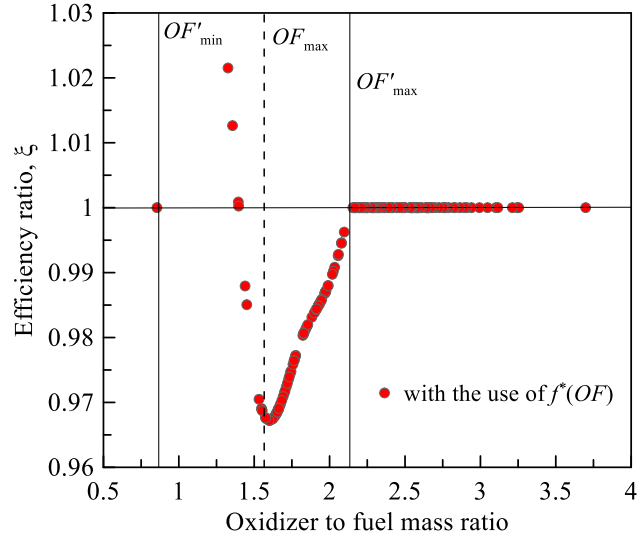

Figure 9 Time history of the efficiency-ratio ξ in the firing F#02.

Note that the indirectly calculated efficiency variation has no physical basis; its functional form only results from the linearization of the actual function f.

Finally, for the sake of comparison, the results obtained in test F#01 are reported in Figure 10. This test, unlike test F#02, yields a variation of the oxidizer-to-fuel mass ratio that spans in the range $[OF_{max}, OF_{min}]$, for which the solution of Eq. (10) must be handled by means of the function $f^*(OF)$ (instead of f). This is clearly seen looking at the right part of the diagram in Figure 10, where this function is plotted in the range of OF achieved in the test. Here the minimum and maximum values of the function g, i.e. g_1 and g_2 which are attained at the beginning and at the end of the test, respectively, are such that the interval $[f_1, f_2] \subset [g_1, g_2]$.
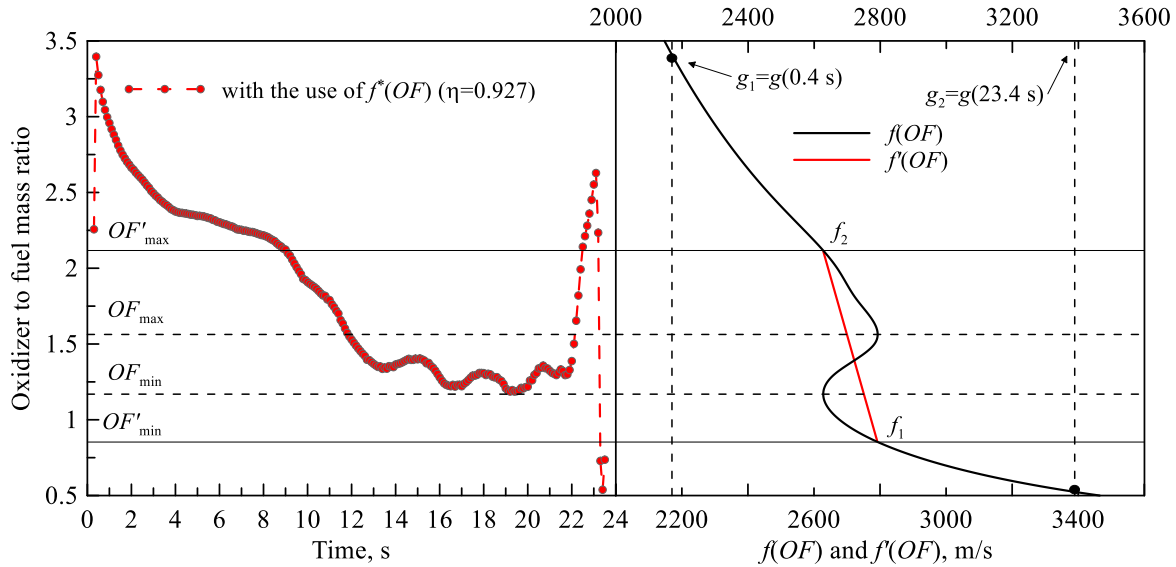

Figure 10 Time history in the firing F#01 of the oxidizer to fuel mass ratio with the details of the ballistic problem solution.

16

4. Experimental Results

The average parameters measured in the experimental tests are listed in Table 3. The effective initial port diameter was measured after removing the central rod from the casing. The data measurement uncertainty has been evaluated according to the procedure in Ref. [10]; regression rate, mixture ratio, total mass flux and mean port diameter uncertainties are, respectively, around 3%, 4%, 3% and 1%. In the following, only regression rate and total mass flux are reported with the relative error bars.

Table 3 Firing tests average results.

Test	D_0, mm	t_b, s	$\bar{m}_{ox}$, kg/s	$\bar{G}_{ox}$, kg/m²s	$\bar{D}$, mm	O/F −	$\bar{r}$, mm/s	$\bar{p}$, MPa	η_0 −	η −
I#01	42.9	6.1	0.020	11.2	47.5	1.98	0.744	0.29	(*)	(*)
I#02	40.2	6.4	0.038	21.5	47.5	2.45	1.140	0.53	(*)	(*)
F#01	40.1	23.2	0.020	7.7	57.5	1.67	0.748	0.32	0.892	0.927
F#02	40.2	19.1	0.030	11.7	57.3	2.07	0.897	0.47	0.901	0.907
F#03	39.8	6.3	0.048	25.0	49.2	2.26	1.498	0.68	0.850	0.855
F#04	40.0	14	0.050	19.9	56.8	2.64	1.205	0.74	0.927	0.923
F#05	40.1	19.3	0.030	11.5	57.3	2.06	0.895	0.46	0.888	0.910

(*) efficiency was not calculated because the measurements of diameter and mass of the fuel grains were affected by larger errors.

The two ignition tests I#01 and I#02, which were carried out with nearly the same burning duration and almost 100% different oxygen mass flow rates, for the different initial diameter (around 7%), yielded equal time-space averaged port diameter of 47.5 mm. In all the firing tests except for F#03 (at the largest mass flux) the average diameter of the port achieved in the firing is about 57 mm. Comparison between ignition tests and firing tests, hence, may allow noting the difference in the regression rate obtained with the same mass flux but different port diameters. The average regression rates are reported versus the total mass flux in Figure 11; here the labels indicate the value of the average port diameter.
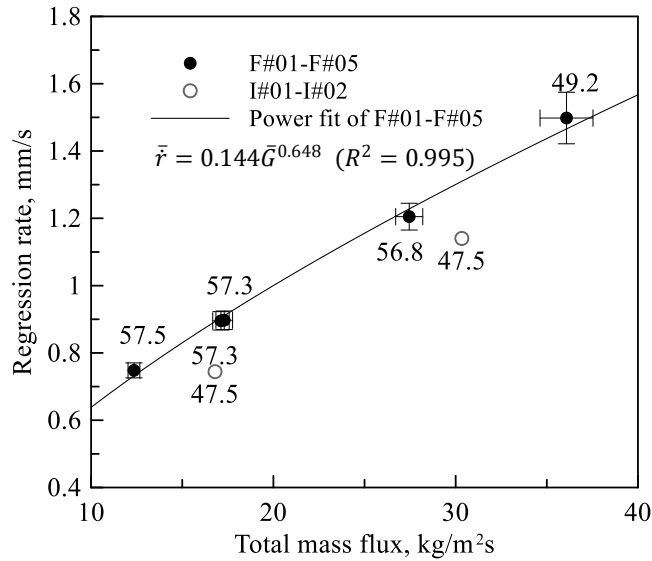

Figure 11 Average regression rate as a function of the total mass flux (labels report average port diameter in mm).

The firing test data points (F#01-F#05) are best fitted with a power function whose parameters are shown in Figure 11; the two points (I#01 and I#02) relative to the smaller diameter of 47.5 mm clearly show lower regression rate at equal mass

flux, which may lead to infer an effect of the oxygen jets discharged from the eight small ports of the axial injector arrangement. In fact, impingement of oxygen on the fuel surface has been pointed out to increase the regression rate also in engine configurations significantly different [36]. As observed in Ref. [36, 37], the mechanism of fuel regression growth with the port diameter is a combination of the increased heat transfer to the wall with the larger liquid wax mechanical entrainment both promoted by the oxidizer jet impingement on the grain surface. An influence of the port diameter on the regression rate was to be expected also from the consideration that, as shown in Figure 8b (despite the oscillations due to the pressure fluctuation) the regression rate is nearly constant with time, displaying only a marginal decrease toward the end of the firing, which clearly involves dependence on an additional parameter other than the mass flux. A correlation with the mass flux and the port diameter is, hence, searched for; the calculated parameters are shown in Figure 12.
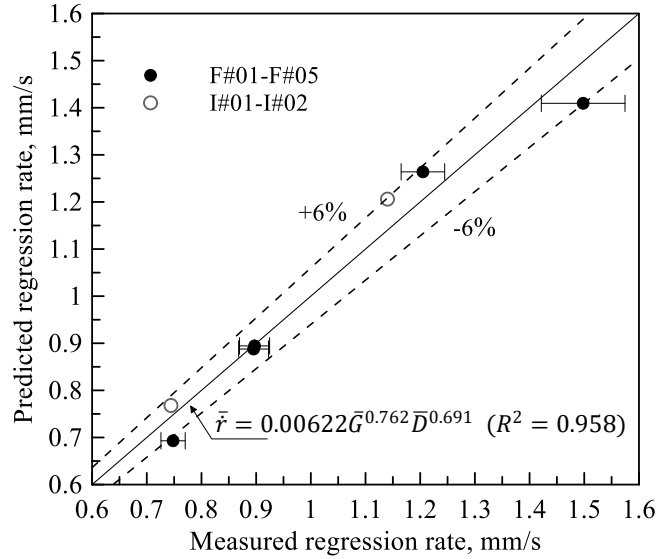

Figure 12 Regression-rate correlation with mass flux and port diameter.

The correlation parameters displayed in Figure 11 and Figure 12 apply with the diameter expressed in mm, mass flux in kg/m^{2}s, and regression rate in mm/s. It is worth remarking that the latter correlation results in a formula that is accurate for the purpose of interpolating the data collected from the analyzed configuration, but cannot be used, without any adjustment, to extrapolate to other scales in that, for the diameter power, it may lead to unrealistically large regression rates. Through the values of the parameters, a, n and m appearing in the two correlations of the form $\dot{r} = aG^nD^m$, it is possible to determine the regression rate at each time step by solving the following algebraic equation

$$\dot{r} = aG_{ox}^n \left(1 + 4\frac{L}{D}\frac{\rho_f \dot{r}}{G_{ox}}\right)^n D^m \qquad (22)$$

in which both the diameter and oxidizer mass flux are known. Based on a usual practice in the hybrid rocket literature [38], starting from average data correlations (which, for their nature, are only an approximation of the time evolution of a given parameter), time-dependent formulas are developed; the port diameter is, thus, calculated from Eq. (22) integrating the regression rate in time by means of Eq. (17). The results of such a procedure are compared in Figure 13.

In Figure 13a the regression-rate time trends obtained with the correlation employing mass flux alone ($m = 0$) and the one involving also the port diameter from the two tests F#02 and I#01 are plotted against the reconstructed data. These two tests are interestingly compared for they yield nearly equal average oxygen mass flux and different port diameters. As

previously observed, test I#01, that features the smaller average port diameter, displays the slower regression rate (see Table 3). The data from both correlations integrated over time, as expected, show a significant decrease that is not observed with the data ballistically reconstructed, which instead show regression rate either growing in test I#01 or nearly constant in test F#02. The regression rate decrease is, of course, milder with the use of the correlation involving both mass flux and port diameter. However, also this latter, which shows in test I#01 an inconsistent decrease, and in test F#02 large deviations at the beginning and at the end of the firing, is unable to reproduce the reconstructed trends. In the two tests the reconstructed fuel mass flow rate increases over the firing (i.e. the oxidizer-to-fuel ratio decreases) and this behavior is completely overshadowed by the correlation with the mass flux alone, and only partially predicted by the other correlation (from the average data correlations one derives that fuel mass flow rate depends on the port diameter roughly as $\dot{m}_f \propto \dot{m}_{ox}^n D^{m-2n+1}$, and if $m - 2n + 1 > 0$ it grows over time).
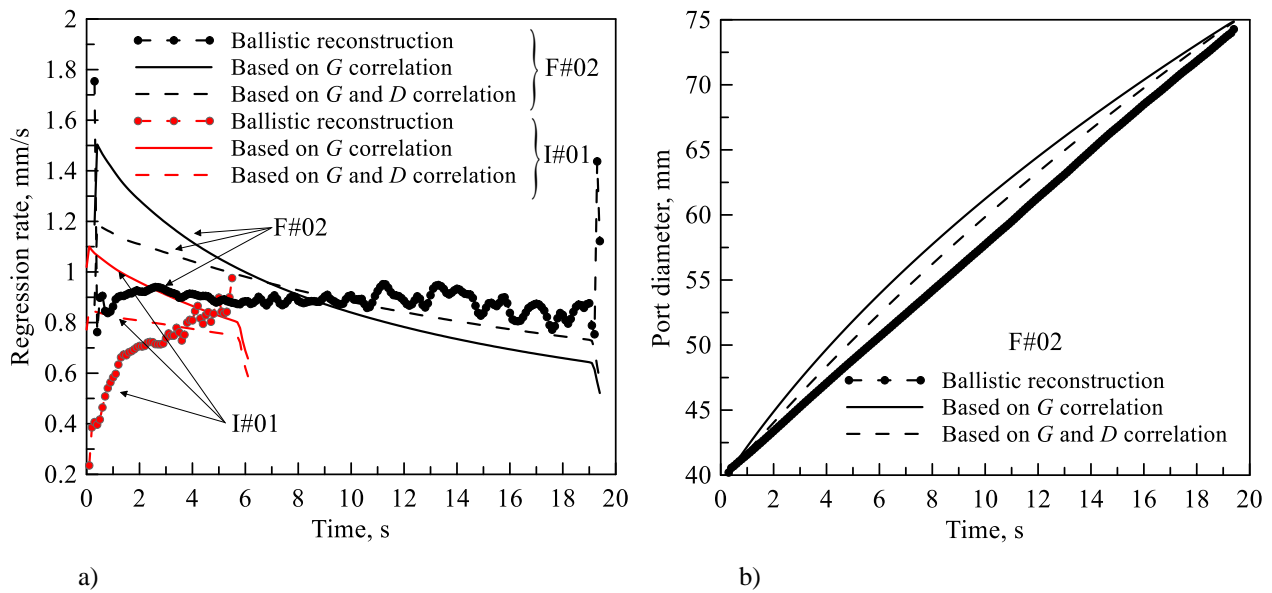

Figure 13 a) Regression rate and b) port diameter histories calculated with the ballistic reconstruction technique and with average data correlations.

In Figure 13b, port diameter histories in test F#02 are plotted. Here the deviations are much lower: notice that, all the three sets of data yield nearly equal time average regression rates (i.e. equal final port diameters), which is because the average regression rate of test F#02 is predicted by both the correlations with negligible deviations (see Figure 11 and Figure 12). A maximum deviation between the port diameter trends of 3.5% is calculated in the middle of the firing.

In conclusion, comparison in Figure 13 does clearly point out the necessity of a method other than the usual time-space averaging to obtain more reliable trends of the fuel mass flow rate and the related rocket performance parameters over the firing. In this context, note that one might use Eq. (22) to estimate the mixture ratio as a function of the port diameter and oxidizer mass flow rate, and calculate the efficiency over time through Eq. (9). The results, of course, are affected by the uncertainty of time-space average regression-rate correlation. Which one of the two methods provides results closer to the reality cannot be established without measuring the efficiency (for instance by means of the engine thrust measurement as in Ref. [29]) or collecting an ideally infinite number of data averaged over single burns. However, keep in mind that the primary objective of the ballistic reconstruction technique is not estimating the efficiency (which, in our model is just a

parameter that guarantees the equality of the measured and calculated consumed fuel masses), but developing a method to obtain the time evolution of the space averaged port diameter.

4.1 RBS Output Data

In this section the port diameter ballistically calculated and the one obtained with the RBS raw data in the test F#02 are contrasted with each other for a preliminary discussion. Data are shown in Figure 14.
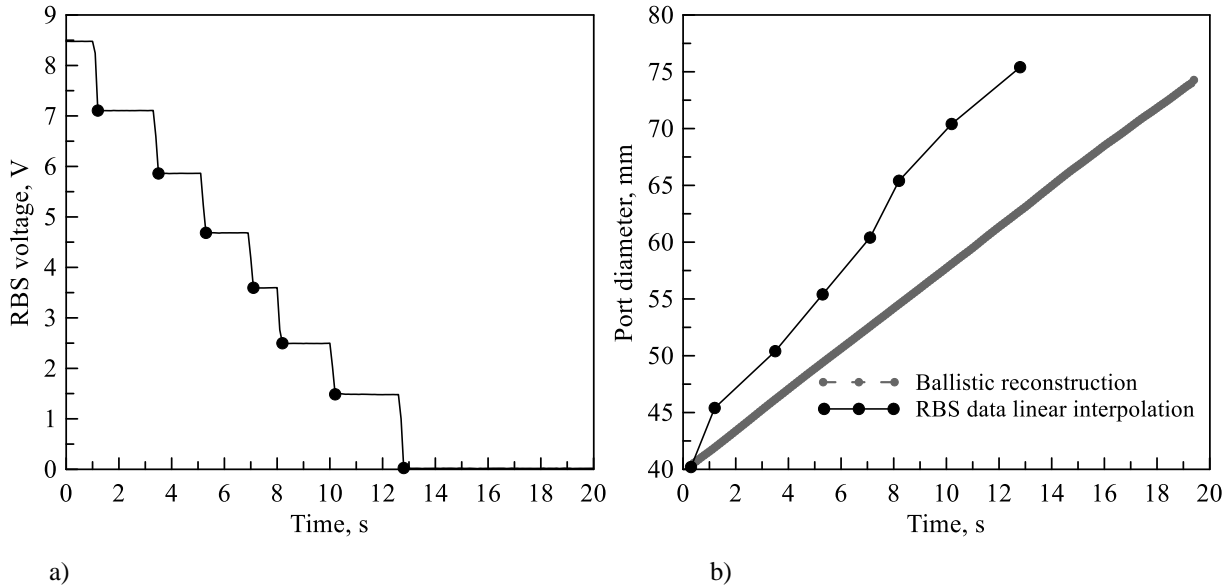

a)   b)

Figure 14 a) RBS output voltage and b) port-diameter time trends obtained with RBS and the ballistic reconstruction in the firing F#02.

The RBS signal (Figure 14 a) displays a time evolution in the form of discrete values, which are related to the position of the single conductors in Figure 1: at the instant when the voltage measured across the measurement resistor R shows an abrupt change, upon breakage of a conductor, the fuel thickness relative to the given conductor position is nominally consumed and the corresponding diameter is shown in the graph (Figure 14 b). Note that each recorded diameter variation is 5 mm, which is equal to the double of the distance between two successive conductors (see Figure 1).

It is clear that the diameter measured with RBS significantly deviates from the one ballistically calculated; the deviation increases over the burn and is maximum at around 13 s when the innermost conductor is broken and the measured diameter is close to 75 mm, whereas that ballistically calculated is around 62.5 mm. A reason for this discrepancy was searched for in the possible unevenness of the axial fuel consumption, for which, at the grain mid length where the RBS is placed, the port diameter could be non-negligibly larger than the average one. The fuel consumption distribution was evaluated by measuring the local after-burn port diameter by means of the technique addressed in Ref. [39], which, in short, consists in measuring the volume of the water progressively poured in the grain and the relative height. Here, the volume measurements were carried out with 5-mm axial step, which implies that the average diameter over 5 mm length is obtained at each measurement point. The associated measurement uncertainty is on the order of 1% [40]. In Figure 15 the fuel port diameter axial profile measured in test F#02 is plotted. Except for the exit section where the flow recirculation at the

backward facing step (see Figure 2) raises the local fuel consumption (see also Figure 16a), the port shape is almost uniform, with a standard deviation of about 5 mm. In the center, where RBS was mounted, fuel port is effectively larger than the average (i.e. the value reached at the end of the burn in Figure 14) with a deviation less than 5 mm, which, thus, cannot explain the difference seen in Figure 14.
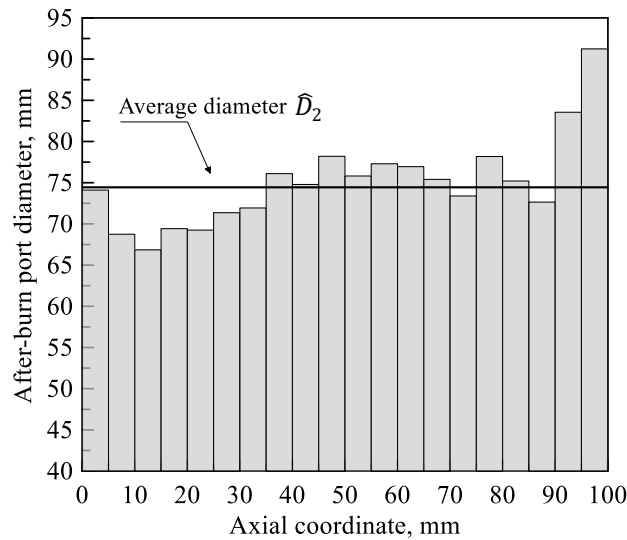

Figure 15 Fuel consumption axial distribution (test F#02).

The inspection of the post-burn grain port shape in the neighborhood of the RBS installation port clearly exhibits increased fuel consumption. As visible in Figure 16, where the picture of the grain inner surface is shown, the zone around the port is approximately circular with about 20-mm diameter, and a depth of roughly 3 mm. This suggests the following two considerations. First, the RBS rigid support made of fiberglass epoxy resin, most likely regresses slower than the surrounding wax, thus sticking out of the inner grain surface; this effect produces a confined region of flow recirculation behind the sensor and raises the local fuel consumption. Second, in this process the conductors on the support are exposed to the flow and, being subjected to larger heat and momentum transfer, break out definitely prior to the paraffin material from all over the grain surface is consumed. The overall result is that, at each time in the firing, the regression rate averaged along the grain is lower than the one in the RBS position, which, in turn, is larger than the RBS conductors' burn rate.
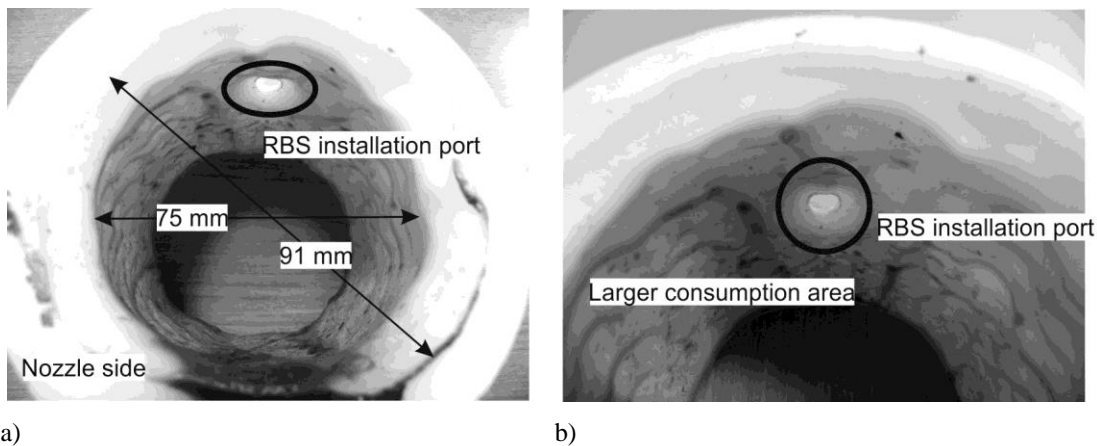

Figure 16 Test F#02, a) post burn fuel grain, b) details of the region where RBS was installed (top of the grain).

4.2 Remarks on the RBS Installation and Raw Data Treatment

The latter observation raised in the previous section is supported by the image of the fuel grain of test F#01 in Figure 17. Here one can see that, after the burn, part of the RBS support still sticks out of the surface, whereas the conductors were burned out in the firing. F#01 was the first engine firing test performed with the sensor installed on the bottom of the casing; wax melted from the top of the grain surface deposited on the bottom as can be seen in Figure 17b. Hence, the next tests were all carried out by rotating the casing of 180° in such a way that the RBS was placed on the top.

Furthermore, in a couple of tests, after the cooling down of the cast fuel grains, the RBS circuit was tested and was found interrupted. This fault was likely due to the wax shrinkage (typically on the order of a couple of millimeters along the axial direction and 1 mm along the inner diameter) for which the conductors were displaced along the support and were broken.
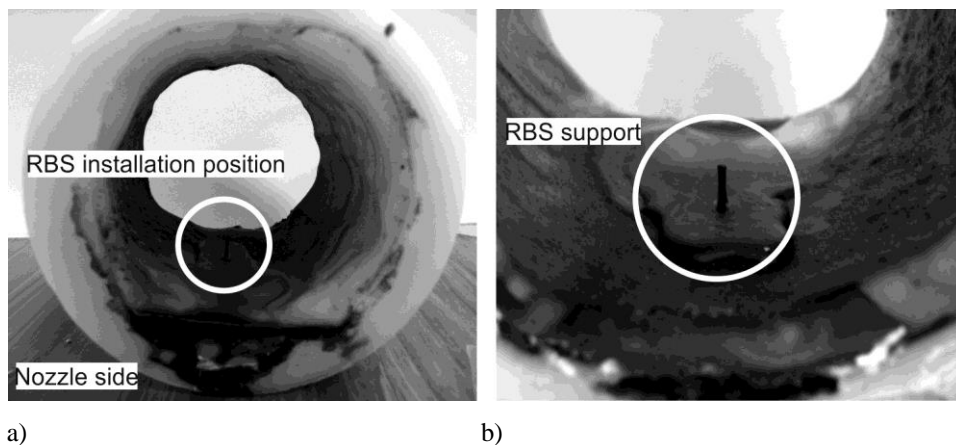

a)   b)

Figure 17 Test F#01, a) post-burn fuel grain, b) details of the melted wax in the region of RBS installation.

At this level of investigation, from the data shown above, one main consideration can be drawn. Being the sensor support made by a material that burns slower than paraffin, one cannot expect to see accurate port diameter measurement without applying any correction to the raw data. With the target of controlling the engine mixture ratio, in principle, at the expense of a number of experimental firings, one should be able to find a transfer function between the RBS data and the average diameter in the port either reconstructed or measured after the burn. For instance, a sort of correlation between the two sets of data in Figure 15 that would allow evaluating the average diameter of the grain from the sensor raw outputs. However, this observation only highlights the need for further study on a real application of such a kind of sensors.

5. Conclusions

A series of static firings of a small-scale hybrid rocket engine burning gaseous oxygen and microcrystalline-wax based fuel was conducted with the purpose of preliminarily investigate in the feasibility of employing an existing version of a resistor-based sensor to measure the fuel regression rate over time. This inquiry unfolds from the need of a fuel mass flow rate real-time measurement technique allowing for the control of the oxidizer-to-fuel ratio in an A-SOFT hybrid engine. To provide a base for comparison with measured data and, more in general, to build up a simple and useful framework for reconstructing time-resolved space-averaged regression rate, an existing ballistic technique was reconsidered and revised. This latter makes use of the time histories of the engine aft-chamber pressure and oxidizer mass flow rate measurement,

along with the post burn total fuel mass consumed, to estimate the average combustion efficiency as well as the regression rate and port diameter time trends. The novelty of the analysis carried out in this paper is that it was demonstrated that, whatever the propellant combination is, in the left interval of the optimum characteristic-velocity mixture ratio (around which the engine is usually designed), the lumped-parameters continuity equation across the combustion chamber, under the assumption of constant efficiency with time, does admit three distinct solutions in terms of fuel mass flow rate. Moreover, it was shown that the problem of multiple solutions can be solved by a proper root-tracking method, provided that the pressure-to-oxidizer mass flow rate ratio excursion in the firing satisfies certain conditions. However, in case those conditions are not met, a particular variation of the efficiency was proposed which ensures to uniquely solve the problem. The ballistically reconstructed data showed that regression rate remains nearly constant in the firing, despite the average data yielded a clear dependence on the total mass flux (which, of course, decreases over time). The reason seems to be an effect of the port diameter caused by the impingement on the fuel surface of the oxygen jets ensuing from the circumferential ports of the injector, which increases both the heat transfer to the fuel and the mechanical entrainment of the liquid layer forming on the surface. As inferred from the average data, with equal total mass flux, the larger is the port diameter, the higher is the achieved regression rate. However, even considering the effect of the diameter calculated with the average data, the derived time-resolved regression rate is not accurately reproduced, which undoubtedly proves the need for a ballistic method.

With the aid of the reconstructed space-averaged port diameter, a comparison to the raw data coming from the RBS was drawn. This combined analysis showed that the sensor-measured diameter is considerably larger than the reconstructed one, even considering the non-uniform axial fuel consumption. This behavior is likely caused by the characteristics of the current RBS electrical conductors' support. With burning slower than the paraffin fuel, the sensor support generated a local recirculating flow in turn creating thermal and mechanical stresses that broke the RBS wires. As a final result, the wire-cut sensor captured an increased regression rate with respect to the mass balance method used as a starting point of the analysis. The main outcome of the preliminary analysis presented in this paper is that, if one would rely on an RBS for the mixture-ratio control in a rocket fuelled with paraffin wax, in the absence of a support material with a melting point similar to the paraffin's one, a transfer function needs to be determined between the raw data and the average port diameter. This is the subject of next analyses.

Appendix A: On the effect of the curve selection upon the reconstructed ballistic data

The ballistically reconstructed mixture ratio as well as all the derived data are affected by the particular curve that is assumed to substitute the original function $f(OF)$ diagram in the range $[OF'_{min}, OF'_{max},]$; this effect is the subject of this appendix. The results obtained in test F#01 are analyzed as an example; as noted in Sec. 3.2, in this firing test the time-resolved oxidizer-to-fuel mass ratio varies all over the range $[OF_{max}, OF_{min}]$, hence a monotonic decreasing function, which replaces f in the aforementioned range, is required for the solution of Eq. (10). The diagram of the function $f(OF)$ obtained at 0.32 MPa (that is the average pressure in F#01, see Table 3) is shown in Figure A 1. Because of the different chamber pressure of F#01 the characteristic values appearing in the picture are slightly different from those in Figure 6 and are listed in Table A 1.
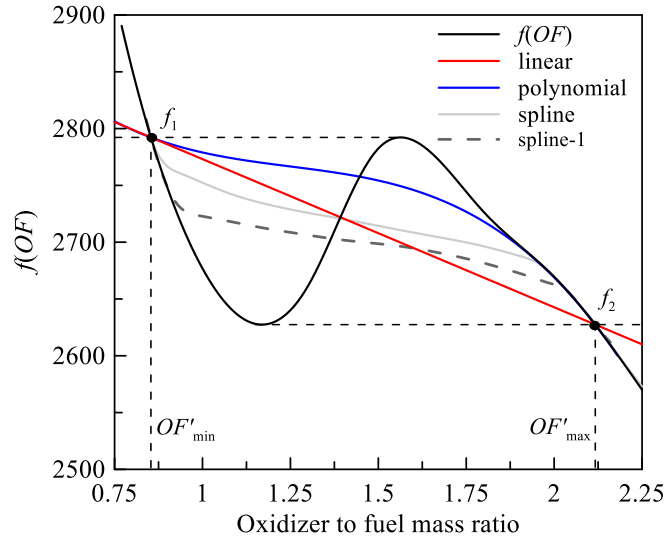
Figure A 1 Graphical representation of the substitution of *f(OF)* with three distinct curves in the firing F#01.

Here, three distinct curves have been selected: a third order polynomial (blue line in Figure A 1), and two curves constructed by points interpolated with cubic splines, one of which (i.e. "spline" in Figure A 1) passes through the intersection of the linear function (red line) and *f(OF)*. All the curves pass through the two points $[OF'_{min}, f_1,]$ and $[OF'_{max}, f_2]$; furthermore the polynomial has the same first derivative as *f* in OF'_{max}, and the constant term such that it is monotonically decreasing in the selected range; the relevant equation, $\wp(OF)$, is:

$$\wp(OF) = a \cdot OF^3 + b \cdot OF^2 + c \cdot OF + d \tag{A1}$$

in which all the coefficients are expressed in m/s and their values are as follows: $a = -161.1$, $b = 603.8$, $c = -793.7$, and $d = 3130$. Note that there is no third order polynomial strictly decreasing in the range $[OF'_{min}, OF'_{max},]$ whose first derivative in OF'_{min} is equal to that of *f*.

Table A 1 Characteristic values the function *f(OF)* assumes in the firing F#01

OF'_{min}	OF_{min}	OF_{max}	OF'_{max}	f_1	f_2
0.853	1.169	1.563	2.117	2792.2	2627.4

The selected curves, of course, represent only three of the infinite chances one can have in assuming suitable decreasing functions between f_1 and f_2. The effect of the particular functional shape is shown in Figure A 2, where the oxidizer-to-fuel mass ratio, space-averaged regression rate and port diameter time histories are reported; refer to Figure 10 for detailed results coming from assuming the linear function substitute for *f(OF)*.
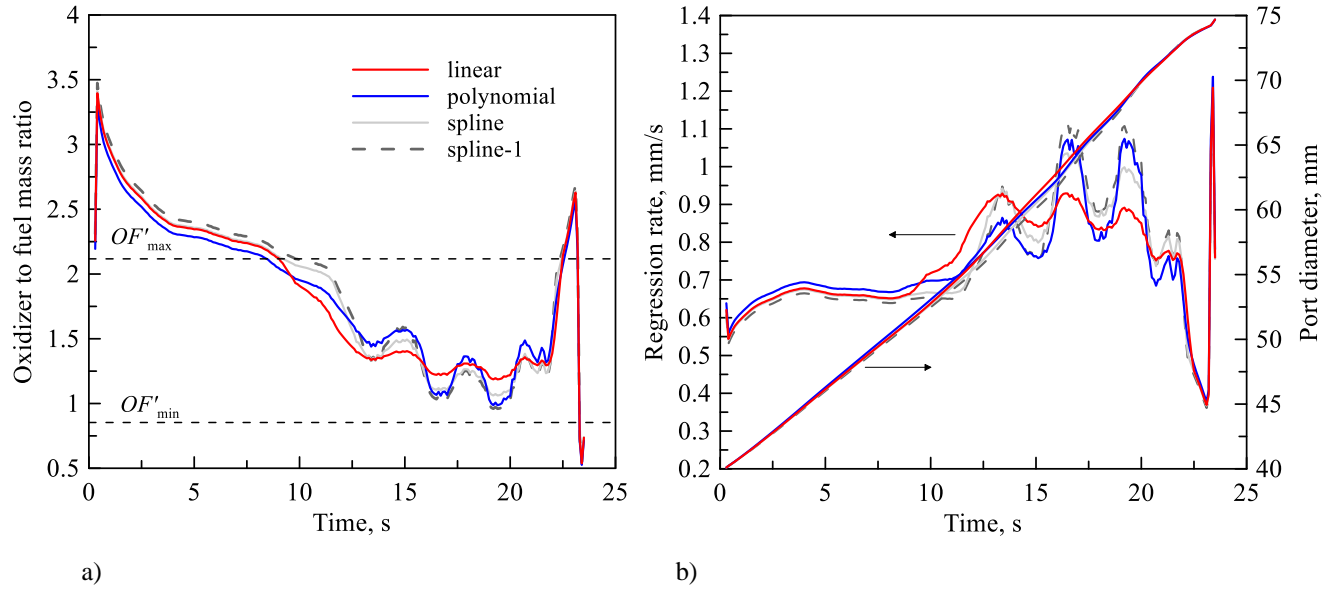
Figure A 2 Comparison of time histories in the firing F#01 of a) oxidizer to fuel mass ratio, b) regression rate and port diameter.

First, note that even outside the range [OF'_{min}, OF'_{max},] (where there is no substitution of the function f) the four sets of ballistically reconstructed data differ from each other because of the different values of the calculated efficiency, which guarantee that the determined fuel mass consumed in each case is equal to the measured one and, therefore, the consistency of the mean O/F. The percent deviations of the calculated efficiencies relative to the case of the linear function selection (for which $\eta = 0.927$) are listed in Table A 2; the maximum difference is yielded when the polynomial function is used and is around 1%. By defining OF_{ave} the arithmetic average of the time-resolved reconstructed oxidizer-to-fuel mass ratio:

$$OF_{ave} = \sum_{i=1}^{N} OF_i \neq O/F \tag{A2}$$

one can see in Table A 2 that also this parameter is not significantly sensitive to the specific curve, though the maximum deviation can be up to 21.2% (displayed by the spline-1). Accordingly, regardless of the specific curve used, all the sets of data meet the condition that the propulsive parameters averaged over the burn negligibly change.

Table A 2 Maximum percent deviation relative to the linear function over the burn in the firing F#01

	Polynomial	Spline	Spline-1
Mixture ratio	12.5	18.6	21.2
Regression rate	20.5	12.0	24.2
Port diameter	0.09	0.09	0.09
Efficiency	-1.08	0.22	0.97
OF_{ave}	-0.13	1.27	2.61

Regression rate is affected by the largest deviations, as expected from the arguments explained with the support of Eq. (20). Finally, in Figure A 3 the efficiency calculated with the four curves is depicted versus the corresponding mixture ratio. From that picture, one can clearly see that the curve shifting less from the original f diagram results in a wider range where

the efficiency is constant; this is shown, in particular, by the polynomial that practically coincides with f from $OF'_{\max}$ up to $OF \cong 1.8$ (see Figure A 1). With this in mind, the linear function is the one leading to the largest variation of the efficiency; thus, one may find the curve decreasing in $[OF'_{\min}, OF'_{\max},]$ which is the closest to f in a least-squared sense. However, without experiments aimed at measuring the real variation of the efficiency in the firing, there is no reason to believe that this hypothetical curve would be the best choice.
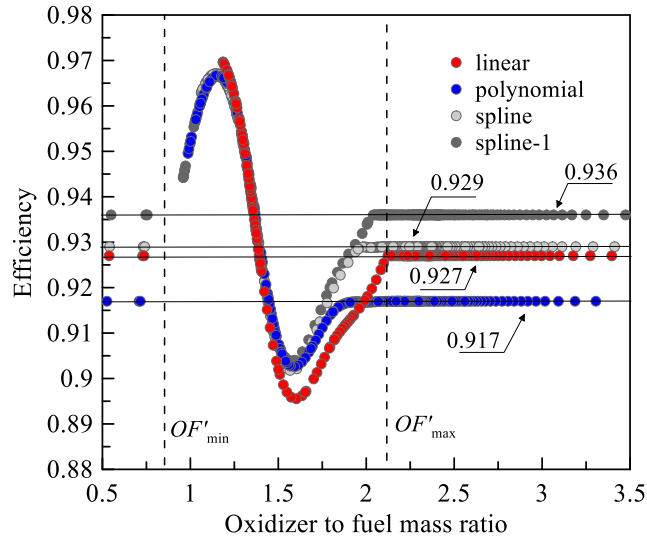

Figure A 3 Comparison of the efficiencies calculated in the firing F#01.

Acknowledgments

References

[1] Altman, D., and Humble, R., "Hybrid Rocket Propulsion Systems," *Space Propulsion Analysis and Design*, edited by R. W. Humble, G. N. Henry, and W. J. Larson, 1st Ed., McGraw–Hill, New York, 1995, pp. 365–370.

[2] Altman, D., "Overview and History of Hybrid Rocket Propulsion," *Fundamentals of Hybrid Rocket Combustion and Propulsion*, Edited by Martin J. Chiaverini, and Kenneth K. Kuo, Progress in Astronautics and Aeronautics, Vol. 218, AIAA, 2007, pp. 1-36.

[3] Schmierer, C., Kobald, M., Tomilin, K., Fischer, U., Schlechtriem, S., "Low cost small-satellite access to space using hybrid rocket propulsion," *Acta Astronautica*, Vol. 159, 2019, pp. 578–583.

doi: 10.1016/j.actaastro.2019.02.018

[4] Jens, E.T., Cantwell, B.J., Hubbard, G.S., "Hybrid rocket propulsion systems for outer planet exploration missions," *Acta Astronautica*, Vol. 128, 2016, pp. 119–130.

doi: 10.1016/j.actaastro.2016.06.036

[5] Pastrone, D., and Casalino, L., "Optimal Robust Design of Hybrid Rocket Engines," *Space Engineering Modeling and Optimization with Case Studies,* edited by G. Fasano and J.D. Pinter. Springer, 2016, pp. 269-285. ISBN 978-3-319-41508-6.

[6] Kuo, K. K. and Houim, R. W., "Theoretical Modeling and Numerical Simulation Challenges of Combustion Processes of Hybrid Rockets," AIAA Paper 2011-5608, 2011.

doi: https://doi.org/10.2514/6.2011-5608

[7] Di Martino, G.D., Carmicino, C., Mungiguerra, S., Savino, R., "The Application of Computational Thermo-Fluid-Dynamics to the Simulation of Hybrid Rocket Internal Ballistics with Classical or Liquefying Fuels: A Review," *Aerospace*, 2019, Vol. 6, No. 5, 56.

doi: https://doi.org/10.3390/aerospace6050056

[8] Chiaverini, M. J., Serin, N., Johnson, D. K., Lu, Y. C., Kuo, K. K., and Risha, G. A., "Regression Rate Behavior of Hybrid Rocket Solid Fuels," *Journal of Propulsion and Power*, Vol. 16, No. 1, 2000, pp. 125–132.

doi: https://doi.org/10.2514/2.5541

[9] Carmicino, C. and Russo Sorge, A., "Role of Injection in Hybrid Rockets Regression Rate Behavior," *Journal of Propulsion and Power*, Vol. 21, No. 4, 2005, pp. 606–612.

doi: https://doi.org/10.2514/1.9945

[10] Carmicino, C. and Russo Sorge, A., "Experimental Investigation into the Effect of Solid-Fuel Additives on Hybrid Rocket Performance," *Journal of Propulsion and Power*, Vol. 31, No. 2, 2015, pp. 699–713.

doi: https://doi.org/10.2514/1.B35383

[11] Evans, B., Risha, G. A., Favorito, N., Boyer, E.,Wehrman, R. B., Libis, N., and Kuo, K. K., "Instantaneous Regression Rate Determination of a Cylindrical X-Ray Transparent Hybrid Rocket Motor," AIAA Paper 2003-4592, July 2003.

doi: https://doi.org/10.2514/6.2003-4592

[12] Russo Sorge, A., and Quaranta, G., "Regression Rate Measurement Methods in Hybrid Motors," Measurement of Thermophysical and Ballistic Properties of Energetic Materials, Politecnico di Milano, Milano, Italy, 23-24 Jun., 1998

[13] Gramer, D. J., and Taagen, J.T., "Material Regression Sensor," US Patent 6,590,403, 2003

[14] Thomas, J. C., Petersen, E. L., De Sain, J., and Brady, B. B., "Hybrid Rocket Burning Rate Enhancement by Nano-Scale Additives in HTPB Fuel Grains," AIAA Paper 2014-3995, July 2014

doi: https://doi.org/10.2514/6.2015-4041

[15] Maggi, F., Galfetti, L. and Colombo, G. Regression Sensor for a Solid Material. Patent; International Publication Number WO2015011100A1, 2015.

[16] Messineo, J., Kitagawa, K. and Shimada, T. O/F Ratio Measurement for Hybrid Rocket Engine Feedback Control. 15th International Conference on Flow Dynamics (ICFD); Sendai, Japan, 2018.

[17] Messineo, J., Shimada, T., "Theoretical Investigation on Feedback Control of Hybrid Rocket Engines," *Aerospace*, 2019, Vol. 6, No. 6, 65.

doi: https://doi.org/10.3390/aerospace6060065

[18] Karabeyoglu, A., Zilliac, G., Cantwell, B.J., De Zilwa, S., and Castellucci, P., "Scale-Up Tests of High Regression Rate Paraffin-Based Hybrid Rocket Fuels," *Journal of Propulsion and Power*, Vol. 20, No. 6, 2004, pp. 1037-1045.

doi: https://doi.org/10.2514/1.3340

[19] Chandler, A., Jens, E., Cantwell, B. J., and Hubbard, G. S., "Visualization of the Liquid Layer Combustion of Paraffin Fuel for Hybrid Rocket Applications," AIAA paper 2012-3961, July 2012.

doi: https://doi.org/10.2514/6.2012-3961

[20] Petrarolo, A., and Kobald, M., "Evaluation Techniques for Optical Analysis of Hybrid Rocket Propulsion," *Journal of Fluid Science and Technology*, Vol. 11, No. 4, 2016, pp. 1-20.

doi: https://doi.org/10.1299/jfst.2016jfst0028

[21] Kobald, M., Schmierer, C., Ciezki, H. K., Schlechtriem, S., Toson, E., and De Luca, L. T., "Viscosity and Regression Rate of Liquefying Hybrid Rocket Fuels," *Journal of Propulsion and Power*, Vol. 33, No. 5, 2017, pp. 1245-1251.

doi: https://doi.org/10.2514/1.B36207

[22] Veale, K., Adali, S., Pitot, J., and Brooks, M., "A Review of the Performance and Structural Considerations of Paraffin Wax Hybrid Rocket Fuels With Additives," *Acta Astronautica*, Vol. 141, December 2017, pp. 196–208.

doi: https://doi.org/10.1016/j.actaastro.2017.10.012

[23] Nakagawa, I., Hikone, S., "Study on the Regression Rate of Paraffin-Based Hybrid Rocket Fuels," *Journal of Propulsion and Power*, Vol. 27, No. 6, 2011, pp. 1276– 1279.

doi: https://doi.org/10.2514/1.B34206

[24] Gordon, S., McBride, B.J., "Computer program of complex chemical equilibrium compositions and applications", NASA Reference Publication 1311, 1994.

[25] Wernimont, E. J., and Heister, S. D., "Reconstruction Technique for Reducing Hybrid-Rocket Combustion Test Data," *Journal of Propulsion and Power*, Vol. 15, No. 1, 1999, pp. 128–136.

doi: https://doi.org/10.2514/2.5401

[26] George, P., Krishnan, S., Varkey, P. M., Ravindran, M., and Ramachandran, L., "Fuel Regression Rate in Hydroxil-Terminated-Polybutadiene/Gaseous Oxygen Hybrid Rocket Motors," *Journal of Propulsion and Power*, Vol. 17, No. 1, 2001, pp. 35–42.

doi: https://doi.org/10.2514/2.5704

[27] Kumar, R., Ramakrishna, P.A., "Measurement of Regression Rate in Hybrid Rocket Using Combustion Chamber Pressure," *Acta Astronautica*, Vol. 103, 2014, pp. 226-234.

doi: https://doi.org/10.1016/j.actaastro.2014.06.044

[28] Nagata, H., Nakayama, H., Watanabe, M., Wakita, M., Totani, T., "Accuracy and Applicable Range of a Reconstruction Technique for Hybrid Rockets," *Advances in Aircraft and Spacecraft Science*, Vol. 1, No. 3, 2014, pp. 273-289.

doi: https://doi.org/10.12989/aas.2014.1.3.273

[29] Carmicino, C., and Russo Sorge, A., "Influence of a Conical Axial Injector on Hybrid Rocket Performance," *Journal of Propulsion and Power*, Vol. 22, No. 5, 2006, pp. 984-995.

doi: https://doi.org/10.2514/1.19528

[30] Carmicino, C., and Pastrone, D., "Novel Comprehensive Technique for Hybrid Rockets Experimental Ballistic Data Reconstruction," *Journal of Propulsion and Power*, Vol. 34, No. 1, 2018, pp. 133-145.

doi: https://doi.org/10.2514/1.B36517

[31] Carmicino, C., "Acoustics, Vortex Shedding, and Low-Frequency Dynamics Interaction in an Unstable Hybrid Rocket," *Journal of Propulsion and Power*, Vol. 25, No. 6, 2009, pp. 1322-1335

doi: https://doi.org/10.2514/1.42869

[32] Hill, P. G., Peterson, C. R., "Chemical Rocket Thrust Chambers," Mechanics and Thermodynamics of Propulsion, 2nd Ed. Addison - Wesley Publishing Company, Inc., 1992, pp. 534-536.

[33] Lide, D. R., CRC Handbook of Chemistry and Physics, 90th Ed., Boca Raton, Florida, 2009

[34] Cox, J.D., Pilcher, G., Thermochemistry of Organic and Organometallic Compounds, Academic Press, New York, 1970, 1-636.

[35] Saito, Y., Uematsu, T., Isochi, H., Wakita, M., Totani, T., and Nagata, H., "Estimation of Hybrid Rocket Nozzle Throat Erosion History," Transactions of the Japan Society for Aeronautical and Space Sciences, Aerospace Technology Japan, Vol. 14, No. ists30, pp. Pa_145-Pa_151, 2016.

doi: https://doi.org/10.2322/tastj.14.Pa_145

[36] Di Martino, G.D., Mungiguerra, S., Carmicino, C., Savino, R., Cardillo, D., Battista, F., Invigorito, M., and Elia G., "Two-Hundred-Newton Laboratory-Scale Hybrid Rocket Testing for Paraffin Fuel-Performance Characterization," *Journal of Propulsion and Power*, Vol. 35, No. 1, 2019, pp. 224-235.

doi: https://doi.org/10.2514/1.B37017

[37] Di Martino, G. D., Gallo, G., Mungiguerra, S., Carmicino, C., Savino, R., Cardillo, D., Battista, F., "Recent advancements in experimental and numerical characterization of paraffin-based fuels for hybrid rocket application," AIAA Paper 2019-4195, 2019.

doi: https://doi.org/10.2514/6.2019-4195

[38] Karabeyoglu, M. A., Cantwell, B. J., and Zilliac, G., "Development of Scalable Averaged Regression Rate Expressions for Hybrid Rockets," *Journal of Propulsion and Power*, Vol. 23, No. 4, 2007, pp. 737–747.

doi: https://doi.org/10.2514/1.19226

[39] Ozawa, K., Kitagawa, K., Aso, S., Shimada, T., "Hybrid Rocket Firing Experiments at Various Axial–Tangential Oxidizer-Flow-Rate Ratios," *Journal of Propulsion and Power*, Vol. 35, No. 1, 2019, pp. 94-108.

doi: https://doi.org/10.2514/1.B36889

[40] Naka, G., Messineo, J., Kitagawa, K., Carmicino, C., Shimada, T., "Evaluation of Laser-Ranging Method Error in Time-Averaged Fuel Regression Rate Measurement," The 16th International Conference on Flow Dynamics, (ICFD2019), November 6 - 8, 2019, Sendai, Japan